



Communication

# Synthesis and Characterization of Novel Fe<sub>3</sub>O<sub>4</sub>/PVA/Eggshell Hybrid Nanocomposite for Photodegradation and Antibacterial Activity

Piyush Kumar Gupta <sup>1,\*</sup>, Senthilkumar Palanisamy <sup>2,\*</sup>, Tamilarasi Gopal <sup>3</sup>, Ranjithkumar Rajamani <sup>4</sup>, Soumya Pandit <sup>1</sup>, Somya Sinha <sup>5</sup> and Vijay Kumar Thakur <sup>6,7,8,\*</sup>

- <sup>1</sup> Department of Life Sciences, School of Basic Sciences and Research (SBSR), Sharda University, Greater Noida 201310, Uttar Pradesh, India; soumya.pandit@sharda.ac.in
- <sup>2</sup> Department of Biotechnology, Nehru Arts and Science College, Coimbatore 641105, Tamil Nadu, India
- <sup>3</sup> Department of Biotechnology, Kongunadu Arts and Science College, Coimbatore 641029, Tamil Nadu, India; tamilagopal@gmail.com
- <sup>4</sup> Viyen Biotech LLP, Coimbatore 641031, Tamil Nadu, India; biotechranjith@gmail.com
- <sup>5</sup> Department of Biotechnology, Graphic Era Deemed to Be University, Dehradun 248002, Uttarakhand, India; somya12121993@gmail.com
- <sup>6</sup> Biorefining and Advanced Materials Research Centre, Scotland's Rural College, Edinburgh EH9 3JG, UK
- <sup>7</sup> Department of Mechanical Engineering, School of Engineering, Shiv Nadar University, Noida 201314, Uttar Pradesh, India
- <sup>8</sup> School of Engineering, University of Petroleum & Energy Studies (UPES), Dehradun 248007, Uttarakhand, India
- \* Correspondence: dr.piyushkgupta@gmail.com (P.K.G.); senthilkumar1185@gmail.com (S.P.); Vijay.Thakur@sruc.ac.uk (V.K.T.)



**Citation:** Gupta, P.K.; Palanisamy, S.; Gopal, T.; Rajamani, R.; Pandit, S.; Sinha, S.; Thakur, V.K. Synthesis and Characterization of Novel Fe<sub>3</sub>O<sub>4</sub>/PVA/Eggshell Hybrid Nanocomposite for Photodegradation and Antibacterial Activity. *J. Compos. Sci.* **2021**, *5*, 267. <https://doi.org/10.3390/jcs5100267>

Academic Editor:  
Francesco Tornabene

Received: 30 August 2021  
Accepted: 4 October 2021  
Published: 12 October 2021

**Publisher's Note:** MDPI stays neutral with regard to jurisdictional claims in published maps and institutional affiliations.



**Copyright:** © 2021 by the authors. Licensee MDPI, Basel, Switzerland. This article is an open access article distributed under the terms and conditions of the Creative Commons Attribution (CC BY) license (<https://creativecommons.org/licenses/by/4.0/>).

**Abstract:** In the 21st century, hybrid nanocomposites were widely used in bioelectronic, biosensing, photocatalytic, and biomedical applications. In the present study, we fabricated a novel Fe<sub>3</sub>O<sub>4</sub>/PVA/Eggshell hybrid nanocomposite and physicochemically characterized it using powder XRD, EDS, FTIR, VSM, and HR-TEM analysis. The XRD spectrum revealed the crystalline and FCC configuration of Fe<sub>3</sub>O<sub>4</sub> NPs with average crystal size of 16.28 nm, and the HRTEM image indicates the prepared hybrid nanocomposite is of spherical shape with less agglomeration. This hybrid nanocomposite showed a significant photodegradation property in degrading organic pollutants such as congo red and crystal violet dyes under the sunlight irradiation. In addition, the hybrid nanocomposite also displayed a potent antibacterial property against different Gram +ve and Gram -ve bacterial pathogens. This study provides a significant example in the overview of fabrication of cost effectively, eco-friendly, and multiple-application hybrid nanocomposites through eggshell membrane fibers.

**Keywords:** nanocomposite; antibacterial; photodegradation; eggshell; polyvinyl alcohol; metal nanoparticles

## 1. Introduction

Environmental decontamination by photocatalysis is of great interest to the researchers worldwide for its effective conspicuous process [1]. Recent scientific investigations suggest the effective use of metal-based semiconductors in coalescing various light sources and their enhanced photocatalysis properties in controlling the environmental pollution [2]. Metal oxide-built nanomaterials have been also studied for their ability in resolving the band gap issues in photocatalytic activity by absorbing photons more effectively [3]. Among various metal oxide nanoparticles (NPs), the Fe<sub>3</sub>O<sub>4</sub> NPs are found to be an ideal photocatalyst for their high magnetization, high coercivity, superior photon-absorbing capacity, and strong bonds between the molecules due to the better dipole–dipole interactions [4]. Although these nanostructures show a high degree of agglomeration after synthesis, the polymer

coating on their surface provides excellent stability. Several natural and synthetic polymers have been reported for the development of NPs/polymer nanocomposites [5]. Among these polymers, polyvinyl alcohol (PVA), a water-soluble polymer, subsequently prevents the agglomeration of NPs resulting in their mono-dispersed condition and prevents the NP's oxidation [6]. PVA contains both carbon backbone and hydroxyl groups, which can support the hydrophilic nature of iron oxide nanoparticles [6]. In order to improve the photocatalytic activity against organic pollutants such as dyes, the addition of eggshell components with NPs has been used as an effective dye adsorbent from the aqueous solution. The porous structure of the eggshell helps in the easy adsorption and transfer of reactants in catalysis [7]. Due to the high specific surface area and surface reactive site, nanomaterials showed potential proficiencies towards surface dependent photocatalytic properties [8–11]. The recent review articles by Rokesh et al. (2021) clearly indicate the advantage of using hybrid nanocomposites (bismuth hybrids, cadmium hybrids, calcium hybrids, cerium hybrids, cobalt hybrids, copper hybrids, graphitic carbon nitride hybrids, indium hybrids, iron hybrids, lanthanum hybrids, lead hybrids, manganese hybrids, molybdenum hybrids, nickel hybrids, silver hybrids, strontium hybrids, tin hybrids, titanium hybrids, tungsten hybrids and zinc hybrids) as the photocatalytic for the degradation of antibiotics [12]. Previous reports indicate an enhanced photoabsorbance efficiency of hybrid nanocomposites due to their unique properties such as multiple optical properties, higher surface area, and efficient surface and interface interactions through unique mechanisms [13–15]. Nowadays, the eggshell membrane is considered an extraordinary biological source in the field of materials science and technology. The protein fiber (collagen, sialoprotein osteopontin, etc.) is the main composition of the eggshell membrane, which is utilized as a template in the synthesis of noble metallic nanoparticles and nanocomposites for various applications [16–19]. In addition, the porous structure in eggshell contains calcium carbonate ( $\text{CaCO}_3$ ) and specific efficient clusters such as C-O, C-H and C=O and helps in easy adsorption and transfer of reactants in catalysis [20,21]. In the present study, we have fabricated a novel  $\text{Fe}_3\text{O}_4$ /PVA/eggshell hybrid nanocomposite and displayed its photodegradation and antibacterial activity in controlling water pollution by degrading dyes and reducing the bacterial load.

## 2. Materials and Methods

### 2.1. Synthesis and Physicochemical Characterization of $\text{Fe}_3\text{O}_4$ /PVA/Eggshell Hybrid Nanocomposite

Iron oxide NPs ( $\text{Fe}_3\text{O}_4$ ) were synthesized hydrothermally using the earlier reported procedure [22]. The surface modification of  $\text{Fe}_3\text{O}_4$  NPs was carried out using PVA [5]. The waste eggshells were collected, and their inner membrane was removed. Next, the eggshell was milled into a fine powder and was sieved through a 200-mesh. About 5 g of powdered eggshell was mixed with 6% NaOH solution and sonicated for 30 min. The final mixture was centrifuged and dried at 60 °C for 5 h. Next, the fabrication of hybrid nanocomposite was initiated by adding 100 mg of PVA coated  $\text{Fe}_3\text{O}_4$  NPs and 2 mg of eggshell powder in 10 mL deionized water. The mixture was continuously stirred at room temperature for 2 h. The obtained hybrid nanocomposite was washed and concentrated by centrifugation. Further, the hybrid nanocomposite was calcinated at 40 °C for 1h to eliminate the excess eggshell and dried at 60 °C overnight.

The crystalline nature of hybrid nanocomposite was analyzed by powder XRD (Rigaku Miniflex Diffractometer, Neu-Isenburg, Germany). The elemental composition of hybrid nanocomposite was determined using energy dispersive X-ray spectroscopy (EDS, R Model QuanTax 200, Bruker, Billerica, MI, USA). The functional group analysis in hybrid nanocomposite was carried out by fourier-transform infrared spectroscopy (Shimadzu IR-Prestige- 21, Tokyo, Japan). Next, the morphology and size of the hybrid nanocomposite were analyzed by high resolution transmission electron microscopy (HRTEM, Technai G2, Lonate Pozzolo, Italy) and the magnetization was investigated in the hybrid nanocomposite using a vibrating sample magnetometer (VSM, MicroSense, Lowell, MA, USA).

## 2.2. Photodegradation and Antibacterial Activity

The photodegradation activity of Fe<sub>3</sub>O<sub>4</sub>/PVA/eggshell hybrid nanocomposite was studied using two textile dyes, crystal violet (CV) and congo red (CR). The stock solution of each dye was prepared by adding its 1 mg in 1 L of distilled water. Next, 50 mg of hybrid nanocomposite was added in 100 mL of both dye solutions and mixed thoroughly. During the experiment, a negative control was also kept, i.e., dye solution alone. Further, the hybrid nanocomposite-suspended dye solutions were taken under the sunlight and monitored for 1–5 h. At different time intervals, the aliquots of 3 mL suspension were collected, and the degradation of dyes was analyzed by measuring their absorbance values using a UV–vis spectrophotometer at different wavelengths. Using these absorbance values, the percentages of dye degradation were calculated.

The antibacterial property of the hybrid nanocomposite was evaluated against *B. subtilis*, *E. coli*, and *P. aeruginosa* using the disc diffusion method. In brief, *P. aeruginosa*, *E. coli*, and *B. subtilis* ( $1.5 \times 10^8$  CFU/mL) were cultured on MHA plates. In these plates, the 5 mm diameter wells were punched. The hybrid nanocomposite was dispersed in the distilled water at 1 mg/mL concentration. The wells were loaded with 25, 50, and 100 µg/mL concentrations of hybrid nanocomposite. The zone of inhibition (ZOI) around the well was measured, and the antibacterial activity of hybrid nanocomposite was determined. The MIC values of hybrid nanocomposite were also calculated with the protocols proposed by Clinical and Laboratory Standards Institute [23]. The bacterial cultures were treated with 0.5, 1, 10, 25, 50, 75, and 100 µg/mL concentrations of hybrid nanocomposite and incubated further for 24 h at 37 °C. The optical densities of both untreated and treated bacterial cultures were measured before and after the incubation period at 550 nm. In addition, the MBC values of the hybrid nanocomposite were also calculated in different bacterial cultures. All the experiments were performed three independent times in triplicates (n = 3).

## 3. Results and Discussion

### 3.1. Synthesis and Physicochemical Characterizations of Fe<sub>3</sub>O<sub>4</sub>/PVA/Eggshell Hybrid Nanocomposite

In this study, the Fe<sub>3</sub>O<sub>4</sub>/PVA/eggshell hybrid nanocomposite was synthesized hydrothermally as shown in Figure 1. The prepared nanocomposite showed a dark brown color, which indicated the formation of novel Fe<sub>3</sub>O<sub>4</sub>/PVA/eggshell hybrid nanocomposite solution (Figure 2A). The XRD pattern of Fe<sub>3</sub>O<sub>4</sub>/PVA/Eggshell hybrid nanocomposite is shown in Figure 2A. We observed a series of 2θ characteristic peaks at 30°, 35°, 40°, 43°, 58°, 60°, 62.5°, and 73°, corresponding to (220), (311), (400), (400), (422), (511), (440), and (533) crystal planes, confirming the crystalline and face-centered cubic (FCC) configuration of Fe<sub>3</sub>O<sub>4</sub> NPs. The average crystal size of the hybrid nanocomposite was also calculated using Scherrer's equation, which was 16.28 nm [24]. Next, HRTEM image presented almost the spherical shape of hybrid nanocomposite with less agglomeration (Figure 2B). A particle size distribution in the hybrid nanocomposite's size was observed between 2.10 nm and 10.17 nm. EDS analysis showed the presence of Fe, O, C, Mg, and Ca, indicating the formation of Fe<sub>3</sub>O<sub>4</sub> NPs with the purity of hybrid nanocomposite (Figure 2C). The van der Waals forces and the magnetic attraction among the Fe<sub>3</sub>O<sub>4</sub> NPs may be reason for the less aggregation of the nanoparticles. The CaO was found to be strongly bound on the surface of the Fe<sub>3</sub>O<sub>4</sub>/PVA/eggshell nanocomposite. The weak C and Ca signals may be from the eggshell component, which present on the outer surface of the prepared hybrid nanocomposite. The presence of O and Mg signals are due to the protein compounds that are unbound and adhered with the nanostructure, which were removed by centrifugation followed by repeated washing [25–27].

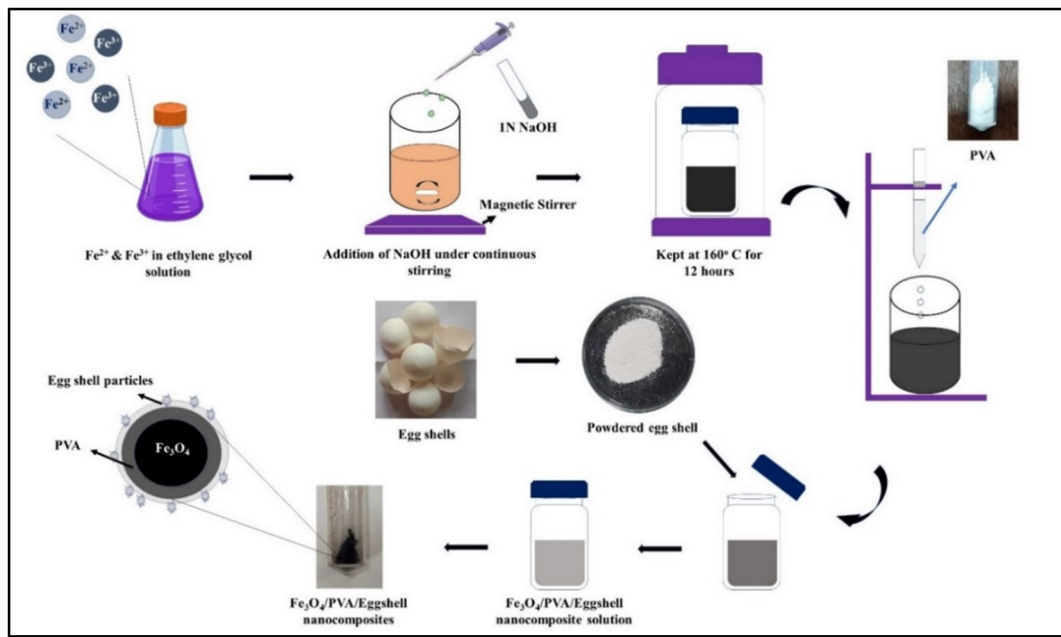


Figure 1. Key steps for the synthesis of Fe<sub>3</sub>O<sub>4</sub>/PVA/eggshell hybrid nanocomposite.

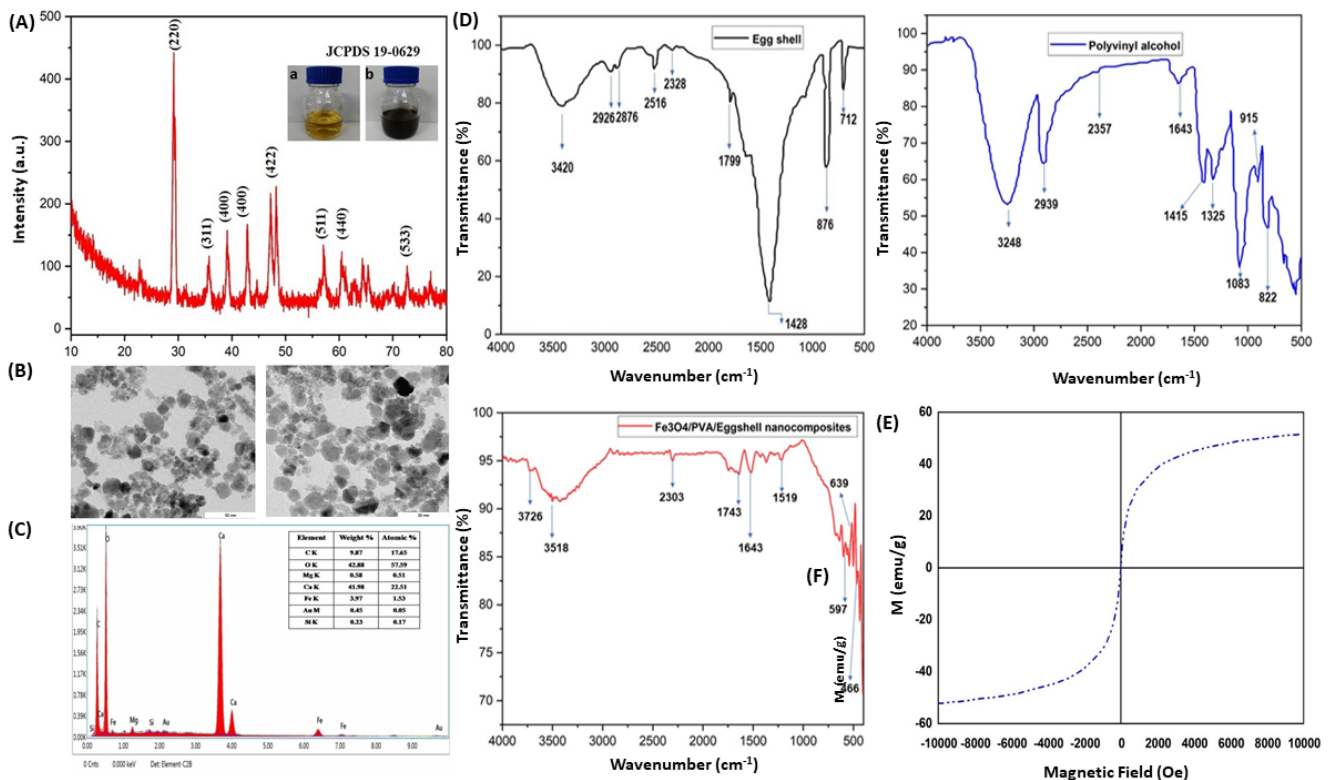


Figure 2. (A) XRD pattern, (B) HR-TEM image on different magnifications (Scale bar—50 nm), (C) EDS analysis, (D) FTIR analysis, and (E) magnetization curve of (F) Fe<sub>3</sub>O<sub>4</sub>/PVA/eggshell hybrid nanocomposite.

The weak signals of C and Ca may be from the eggshell component. Further, FTIR analysis showed the 3420 (OH), 2516 and 2328 (HCO<sub>3</sub>), 1799 (CO), 1428, 712 (C-O), and 876 cm<sup>-1</sup> (OCO) vibrational peaks of eggshell. Similarly, the FTIR spectrum of PVA displayed the peaks at 3248, 2939, 2357, 1663, 1415, 1325, 1083, 915, and 822 cm<sup>-1</sup> for the hydroxyl group, alkyl group, and carbonyl group. The bending vibrations of CH<sub>2</sub> groups congruently related to the functional groups of reduced NPs. The FTIR spectrum

of hybrid nanocomposite exhibited sharp vibrational peaks at 3518, 2303, 1743, 1643, and 1519  $\text{cm}^{-1}$ , corresponding to the hydroxyl group, carbonyl group, alkyl carbonate, carboxylate group, and aromatic nitro compounds, respectively (Figure 2D). The vibration peaks at 639 and 466  $\text{cm}^{-1}$  indicated the iron oxide skeleton and Fe vibrations at tetrahedral site [28]. Similarly, the FTIR analysis of PVA showed the peaks at 3248, 2939, 2357, 1663, 1415, 1325, 1083, 915, and 822  $\text{cm}^{-1}$  corresponding to the hydroxy group (O-H stretching vibrations and H-bonded OH stretch), C-H vibrations of the alkyl group, and C=O vibration of the carbonyl group. The bending vibration related to  $\text{CH}_2$  groups was correspondingly attributed to the functional groups of reduced NPs [29,30]. In the FTIR spectrum of  $\text{Fe}_3\text{O}_4$ /PVA/eggshell, the peak at 639  $\text{cm}^{-1}$  is attributed to the iron oxide skeleton, and the peak at 597  $\text{cm}^{-1}$  corresponds to the aliphatic Iodo compounds and C-I stretch, which is the characteristic of  $\text{Fe}_3\text{O}_4$  NPs. The peak at 466.77  $\text{cm}^{-1}$  is attributed to aryl disulfides (S-S stretch), characteristic of the fundamental stretching vibrations of the Fe at a tetrahedral site. These results were also seen in the previous studies, where a similar characteristic peak was found in the range of 500–600  $\text{cm}^{-1}$  with the iron oxide skeleton [31,32]. The magnetization curve of hybrid nanocomposite is shown in Figure 2E. The symmetrical hysteresis loop indicated the magnetic behavior of  $\text{Fe}_3\text{O}_4$  NPs. The calculated magnetization potential was approximately 54.28 emu/g. In addition, no hysteresis was seen in the magnetization curve, showing its suitability for biological applications. The  $\text{Fe}_3\text{O}_4$  NPs are highly supermagnetic and not ferromagnetic in nature [33].

### 3.2. Photodegradation and Antibacterial Activity

The photodegradation of textile dyes was analyzed by measuring their absorbance values at different time intervals, as shown in Figure 3. The highest absorbance peak was observed at 494 and 592 nm for both CR and CV dyes, respectively. Additionally, hybrid nanocomposite treatment displayed 78 and 73% degradation of CR and CV dyes after 5 h incubation, respectively. Generally, the photodegradation is directly proportional to the exposure time of the dyes with the hybrid nanocomposite. In a previous study, chitosan-S-ZnO nanocomposite exhibited time-dependent photodegradation [34]. In addition, the photocatalytic capacity of the prepared sample was depended on the size and shape of the nanoparticles [35,36].

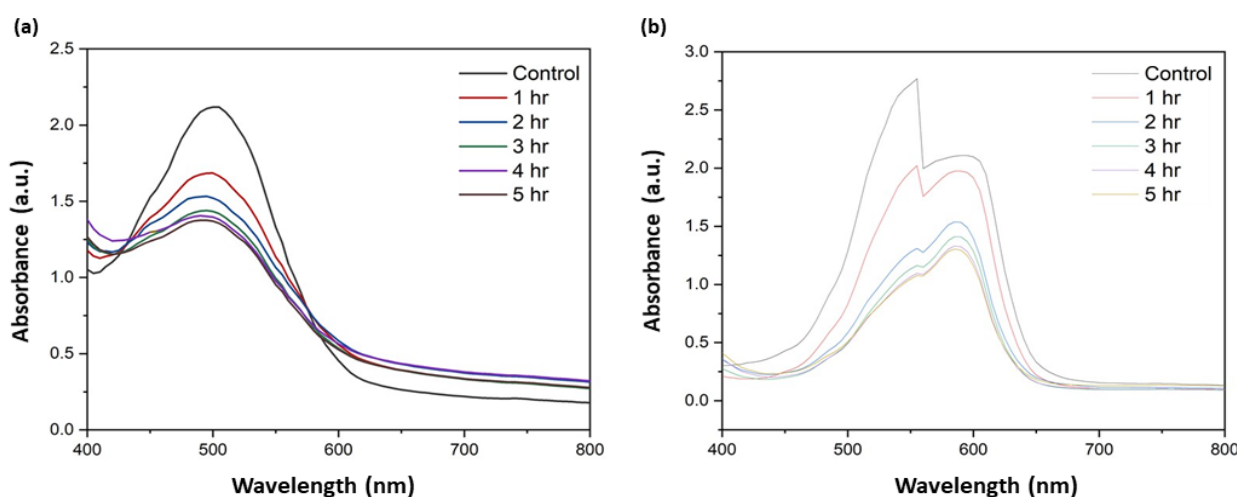


**Figure 3.** Photodegradation of both (a) congo red (CR) and (b) crystal violet (CV) dyes treated with  $\text{Fe}_3\text{O}_4$ /PVA/eggshell hybrid nanocomposite under sunlight irradiation.

Next, the MIC and MBC values of the hybrid nanocomposite were calculated as shown in Figure 4A, and their results showed the hybrid nanocomposite as an effective antibacterial material. The antibacterial activity of the hybrid nanocomposite was also determined using the disc diffusion method by calculating the ZoI values (Figure 4(Ba–c)).

The ZoI values were measured as shown in Figure 4C. High antibacterial activity was identified against *P. aeruginosa* (ZoI =  $23.9 \pm 2.0$  mm), followed by *E. coli* (ZoI =  $23.3 \pm 1.8$  mm), and then *B. subtilis* (ZoI =  $20.2 \pm 2.6$  mm) at 100  $\mu\text{g}/\text{mL}$  concentration of hybrid nanocomposite, whereas the 25  $\mu\text{g}/\text{mL}$  concentration of the hybrid nanocomposite showed the  $2.2 \pm 0.1$ ,  $2.4 \pm 0.2$ , and  $2.1 \pm 0.1$  mm values of ZoI, and 50  $\mu\text{g}/\text{mL}$  concentration of the hybrid nanocomposite showed  $5.9 \pm 0.4$ ,  $9.8 \pm 1.2$ , and  $11.7 \pm 0.8$  mm values of ZoI against *B. subtilis*, *E. coli*, and *P. aeruginosa*, respectively (Figure 4C). The hybrid nanocomposite exhibited the potential antibacterial activity against all tested bacterial pathogens. Generally, the antibacterial activity of nanoparticles can involve several possible mechanisms, such as cell wall synthesis inhibition, inhibition of enzyme, ribosome disassembly, inactivation of protein synthesis, modification of essential proteins, interface with cell signaling, cell surface membrane interaction, formation of ROS, incorporation into the DNA bases to DNA damage, etc. [37–39]. Figure 5 showed the schematic illustration of possible mechanisms of antibacterial activities of nanomaterials [40,41].

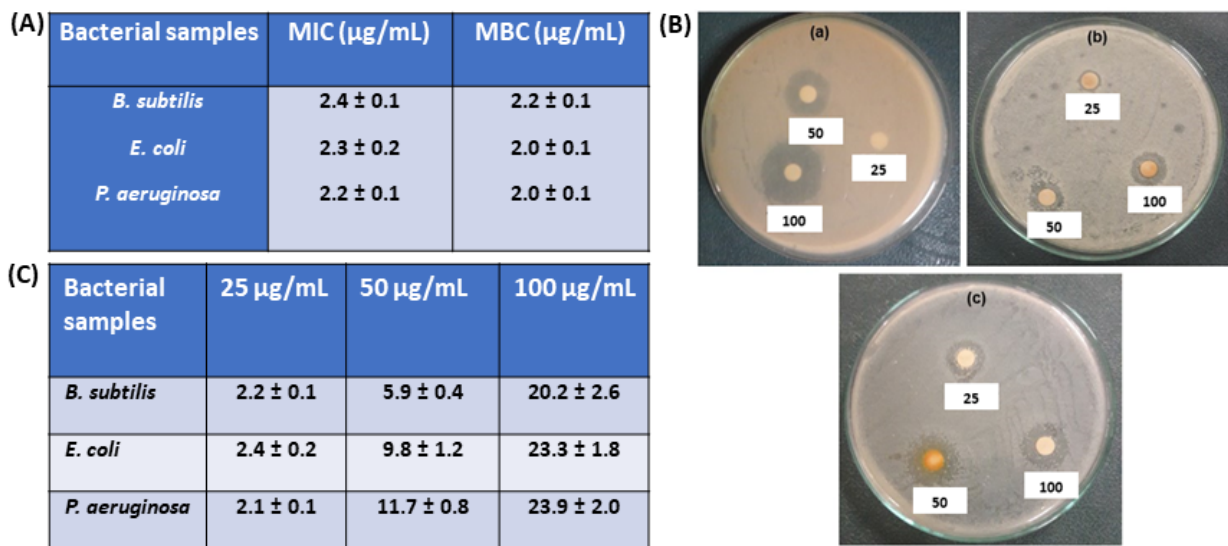


**Figure 4.** (A) MIC and MBC values of hybrid nanocomposite, (Ba–c) antibacterial activity on different concentrations of hybrid nanocomposite against tested (Ba) *P. aeruginosa*, (Bb) *B. subtilis*, and (Bc) *E. coli*. bacterial pathogens, and (C) the calculated ZoI values. The MIC, MBC, and ZoI values are presented as mean  $\pm$  SD.

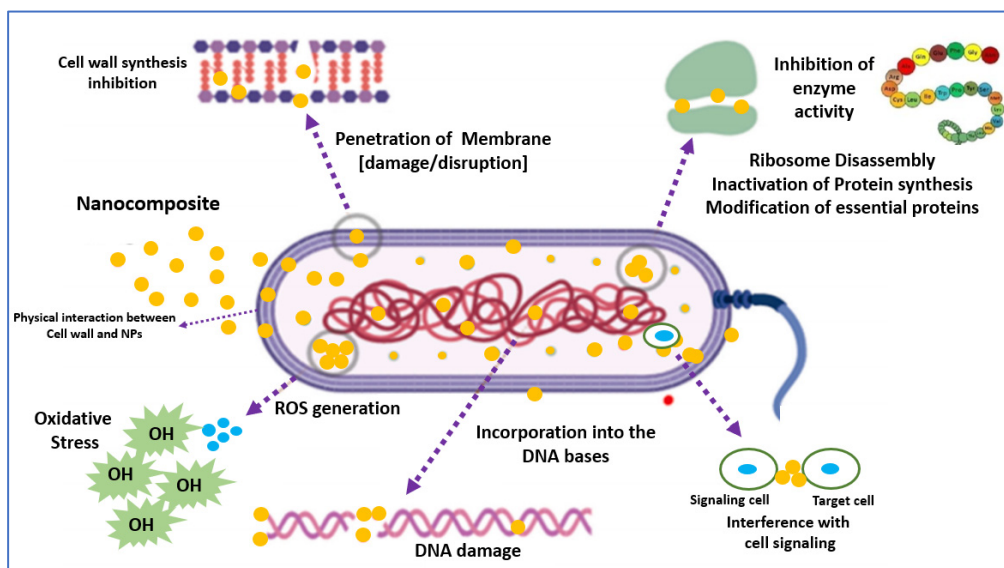


**Figure 5.** Schematic illustration of possible mechanisms of antibacterial activities of nanomaterials [40,41].

#### 4. Conclusions

The present study reports the synthesis and physicochemical characterizations of novel Fe<sub>3</sub>O<sub>4</sub>/PVA/eggshell hybrid nanocomposite. FTIR analysis exhibited the characteristic functional groups of eggshell, PVA, and Fe<sub>3</sub>O<sub>4</sub> NPs in the hybrid nanocomposite. XRD analysis showed the polycrystalline nature of hybrid nanocomposite. FESEM analysis displayed the spherical granules of hybrid nanocomposite. EDS spectrum analysis showed the presence of Fe, O, C, and Ca in hybrid nanocomposite. Further, the hybrid nanocomposite displayed the time-dependent photodegradation property for both CV and CR dyes under sunlight irradiation. In addition, the hybrid nanocomposite also showed the strong antibacterial activity against both Gram-positive and Gram-negative bacterial pathogens.

**Author Contributions:** Conceptualization, writing—original draft preparation, writing—review and editing, P.K.G.; writing—review and editing, T.G., R.R., S.S. and S.P. (Somya Pandit); supervision, project administration, S.P. (Senthilkumar Palanisamy); funding acquisition, supervision, project administration, V.K.T. and P.K.G. All authors have read and agreed to the published version of the manuscript.

**Funding:** This research did not receive any specific grant from the funding agencies in the public, commercial, or not-for-profit sectors.

**Institutional Review Board Statement:** Not applicable.

**Informed Consent Statement:** Not applicable.

**Data Availability Statement:** Not applicable.

**Conflicts of Interest:** The authors declare no competing interests with the work presented in the manuscript.

#### References

1. Sudha, D.; Sivakumar, P. Review on the photocatalytic activity of various composite catalysts. *Chem. Eng. Process. Process. Intensif.* **2015**, *97*, 112–133. [[CrossRef](#)]
2. Liu, L.; Zhang, X.; Yang, L.; Ren, L.; Wang, D.; Ye, J. Metal nanoparticles induced photocatalysis. *Natl. Sci. Rev.* **2017**, *4*, 761–780. [[CrossRef](#)]
3. Chandel, N.; Sharma, K.; Sudhaik, A.; Raizada, P.; Hosseini-Bandegharaei, A.; Thakur, V.K.; Singh, P. Magnetically separable ZnO/ZnFe<sub>2</sub>O<sub>4</sub> and ZnO/CoFe<sub>2</sub>O<sub>4</sub> photocatalysts supported onto nitrogen doped graphene for photocatalytic degradation of toxic dyes. *Arab. J. Chem.* **2019**, *13*, 4324–4340. [[CrossRef](#)]
4. Mishra, P.; Patnaik, S.; Parida, K. An overview of recent progress on noble metal modified magnetic Fe<sub>3</sub>O<sub>4</sub> for photocatalytic pollutant degradation and H<sub>2</sub> evolution. *Catal. Sci. Technol.* **2019**, *9*, 916–941. [[CrossRef](#)]
5. Riva'I, I.; Wulandari, I.O.; Sulistyarti, H.; Sabarudin, A. Ex-Situ Synthesis of Polyvinyl alcohol(PVA)-coated Fe<sub>3</sub>O<sub>4</sub> Nanoparticles by Coprecipitation-Ultrasonication Method. *IOP Conf. Ser. Mater. Sci. Eng.* **2018**, *299*, 12065. [[CrossRef](#)]
6. Kim, S.Y.; Ramaraj, B.; Yoon, K.R. Preparation and characterization of polyvinyl alcohol-grafted Fe<sub>3</sub>O<sub>4</sub> magnetic nanoparticles through glutaraldehyde. *Surf. Interface Anal.* **2012**, *44*, 1238–1242. [[CrossRef](#)]
7. Amarasinghe, A.; Wanniarachchi, D. Eco-Friendly Photocatalyst Derived from Egg Shell Waste for Dye Degradation. *J. Chem.* **2019**, *2019*, 8184732. [[CrossRef](#)]
8. Kumar, A.; Raizada, P.; Hosseini-Bandegharaei, A.; Thakur, V.K.; Nguyen, V.-H.; Singh, P. C-, N-Vacancy defect engineered polymeric carbon nitride towards photocatalysis: Viewpoints and challenges. *J. Mater. Chem. A* **2020**, *9*, 111–153. [[CrossRef](#)]
9. Shubha, J.P.; Savitha, H.S.; Adil, S.F.; Khan, M.; Hatshan, M.R.; Kavalli, K.; Shaik, B. Straightforward Synthesis of Mn<sub>3</sub>O<sub>4</sub>/ZnO/Eu<sub>2</sub>O<sub>3</sub>-Based Ternary Heterostructure Nano-Photocatalyst and Its Application for the Photodegradation of Methyl Orange and Methylene Blue Dyes. *Molecules* **2021**, *26*, 4661. [[CrossRef](#)] [[PubMed](#)]
10. Ates, B.; Koytepe, S.; Ulu, A.; Gürses, C.; Thakur, V.K. Chemistry, Structures, and Advanced Applications of Nanocomposites from Biorenewable Resources. *Chem. Rev.* **2020**, *120*, 9304–9362. [[CrossRef](#)]
11. Raizada, P.; Thakur, P.; Sudhaik, A.; Singh, P.; Thakur, V.K.; Hosseini-Bandegharaei, A. Fabrication of dual Z-scheme photocatalyst via coupling of BiOBr/Ag/AgCl heterojunction with P and S co-doped g-C<sub>3</sub>N<sub>4</sub> for efficient phenol degradation. *Arab. J. Chem.* **2020**, *13*, 4538–4552. [[CrossRef](#)]
12. Rokesh, K.; Sakar, M.; Do, T.-O. Emerging Hybrid Nanocomposite Photocatalysts for the Degradation of Antibiotics: Insights into Their Designs and Mechanisms. *Nanomaterials* **2021**, *11*, 572. [[CrossRef](#)] [[PubMed](#)]
13. Kumar, R.; Raizada, P.; Verma, N.; Hosseini-Bandegharaei, A.; Thakur, V.K.; Van Le, Q.; Nguyen, V.-H.; Selvasembian, R.; Singh, P. Recent advances on water disinfection using bismuth based modified photocatalysts: Strategies and challenges. *J. Clean. Prod.* **2021**, *297*, 126617. [[CrossRef](#)]

14. Hasija, V.; Raizada, P.; Sudhaik, A.; Sharma, K.; Kumar, A.; Singh, P.; Jonnalagadda, S.B.; Thakur, V.K. Recent advances in noble metal free doped graphitic carbon nitride based nanohybrids for photocatalysis of organic contaminants in water: A review. *Appl. Mater. Today* **2019**, *15*, 494–524. [[CrossRef](#)]
15. Sharma, S.; Dutta, V.; Singh, P.; Raizada, P.; Rahmani-Sani, A.; Hosseini-Bandegharai, A.; Thakur, V.K. Carbon quantum dot supported semiconductor photocatalysts for efficient degradation of organic pollutants in water: A review. *J. Clean. Prod.* **2019**, *228*, 755–769. [[CrossRef](#)]
16. Jia, J.; Liu, G.; Yu, J.; Duan, Y. Preparation and Characterization of Soluble Eggshell Membrane Protein/PLGA Electrospun Nanofibers for Guided Tissue Regeneration Membrane. *J. Nanomater.* **2012**, *2012*, 25. [[CrossRef](#)]
17. Wang, Q.; Ma, C.; Tang, J.; Zhang, C.; Ma, L. Eggshell Membrane-Templated MnO<sub>2</sub> Nanoparticles: Facile Synthesis and Tetracycline Hydrochloride Decontamination. *Nanoscale Res. Lett.* **2018**, *13*, 255. [[CrossRef](#)]
18. Sheish, S.G.; Emadi, R.; Ahmadian, M.; Sadeghzade, S.; Tavangarian, F. Fabrication and Characterization of Polyvinylpyrrolidone-Eggshell Membrane-Reduced Graphene Oxide Nanofibers for Tissue Engineering Applications. *Polymers* **2021**, *13*, 913. [[CrossRef](#)]
19. Zheng, B.; Xie, S.; Qian, L.; Yuan, H.; Xiao, D.; Choi, M.M.F. Gold nanoparticles-coated eggshell membrane with immobilized glucose oxidase for fabrication of glucose biosensor. *Sens. Actuators B Chem.* **2011**, *152*, 49–55. [[CrossRef](#)]
20. Nasrollahzadeh, M.; Sajadi, S.M.; Hatamifard, A. Waste chicken eggshell as a natural valuable resource and environmentally benign support for biosynthesis of catalytically active Cu/eggshell, Fe<sub>3</sub>O<sub>4</sub>/eggshell and Cu/Fe<sub>3</sub>O<sub>4</sub>/eggshell nanocomposites. *Appl. Catal. B Environ.* **2016**, *191*, 209–227. [[CrossRef](#)]
21. Guo, Y.; Yang, D.-P.; Liu, M.; Zhang, X.; Chen, Y.; Huang, J.; Li, Q.; Luque, R. Enhanced catalytic benzene oxidation over a novel waste-derived Ag/eggshell catalyst. *J. Mater. Chem. A* **2018**, *7*, 8832–8844. [[CrossRef](#)]
22. Ahmadi, S.; Chia, C.-H.; Zakaria, S.; Saeedfar, K.; Asim, N. Synthesis of Fe<sub>3</sub>O<sub>4</sub> nanocrystals using hydrothermal approach. *J. Magn. Magn. Mater.* **2012**, *324*, 4147–4150. [[CrossRef](#)]
23. Wayne, P. *Performance Standard for Antimicrobial Susceptibility Testing*; 26th Informational Supplement; Clinical and Laboratory Standards Institute (CLSI): Wayne, PA, USA, 2016; Volume 33, p. M100-S23.
24. Senthilkumar, P.; Surendran, L.; Sudhagar, B.; Kumar, D.S.R.S.; Bupesh, G. Hydrothermal assisted Eichhornia crassipes mediated synthesis of magnetite nanoparticles (E-Fe<sub>3</sub>O<sub>4</sub>) and its antibiofilm activity. *Mater. Res. Express* **2019**, *6*, 095405.
25. Takai, Z.I.; Mustafa, M.; Asman, S. Preparation of High-Performance Conductive Polyaniline Magnetite (PANI/Fe<sub>3</sub>O<sub>4</sub>) Nanocomposites by Sol-Gel Method. *Asian J. Chem.* **2018**, *30*, 2625–2630. [[CrossRef](#)]
26. Zhang, P.; Han, Q.; Fan, M.; Jiang, P. Magnetic solid base catalyst CaO/CoFe<sub>2</sub>O<sub>4</sub> for biodiesel production: Influence of basicity and wettability of the catalyst in catalytic performance. *Appl. Surf. Sci.* **2014**, *317*, 1125–1130. [[CrossRef](#)]
27. Helwani, Z.; Ramli, M.; Saputra, E.; Bahruddin, B.; Yolanda, D.; Fatra, W.; Idroes, G.M.; Muslem, M.; Mahlia, T.M.I.; Idroes, R. Impregnation of CaO from Eggshell Waste with Magnetite as a Solid Catalyst (Fe<sub>3</sub>O<sub>4</sub>/CaO) for Transesterification of Palm Oil Off-Grade. *Catalysts* **2020**, *10*, 164. [[CrossRef](#)]
28. Mosaddegh, E.; Hosseininasab, F.A.; Hassankhani, A. Eggshell/Fe<sub>3</sub>O<sub>4</sub> nanocomposite: Novel magnetic nanoparticles coated on porous ceramic eggshell waste as an efficient catalyst in the synthesis of 1,8-dioxo-octahydroxanthene. *RSC Adv.* **2015**, *5*, 106561–106567. [[CrossRef](#)]
29. Andrade, G.; Barbosa-Stancioli, E.F.; Mansur, A.A.P.; Vasconcelos, W.L.; Mansur, H.S. Design of novel hybrid organic–inorganic nanostructured biomaterials for immunoassay applications. *Biomed. Mater.* **2006**, *1*, 221–234. [[CrossRef](#)] [[PubMed](#)]
30. Nasrollahzadeh, M.; Atarod, M.; Sajadi, S.M. Green synthesis of the Cu/Fe<sub>3</sub>O<sub>4</sub> nanoparticles using *Morinda morindoides* leaf aqueous extract: A highly efficient magnetically separable catalyst for the reduction of organic dyes in aqueous medium at room temperature. *Appl. Surf. Sci.* **2016**, *364*, 636–644. [[CrossRef](#)]
31. Senthilkumar, P.; Kumar, D.S.R.S.; Sudhagar, B.; Vanthana, M.; Parveen, M.H.; Sarathkumar, S.; Thomas, J.C.; Mary, A.S.; Kannan, C. Seagrass-mediated silver nanoparticles synthesis by *Enhalus acoroides* and its  $\alpha$ -glucosidase inhibitory activity from the Gulf of Mannar. *J. Nanostruct. Chem.* **2016**, *6*, 275–280. [[CrossRef](#)]
32. Sathishkumar, G.; Logeshwaran, V.; Sarathbabu, S.; Jha, P.; Jeyaraj, M.; Kuberan, R.; Senthilkumar, N.; Sivaramakrishnan, S. Green synthesis of magnetic Fe<sub>3</sub>O<sub>4</sub> nanoparticles using *Couroupita guianensis* Aubl. fruit extract for their antibacterial and cytotoxicity activities. *Artif. Cells Nanomed. Biotechnol.* **2017**, *46*, 589–598. [[CrossRef](#)]
33. Issa, B.; Obaidat, I.M.; Albiss, B.A.; Haik, Y. Magnetic Nanoparticles: Surface Effects and Properties Related to Biomedicine Applications. *Int. J. Mol. Sci.* **2013**, *14*, 21266–21305. [[CrossRef](#)]
34. Haldorai, Y.; Shim, J.-J. Chitosan-Zinc Oxide hybrid composite for enhanced dye degradation and antibacterial activity. *Compos. Interfaces* **2013**, *20*, 365–377. [[CrossRef](#)]
35. Amano, F.; Ishinaga, E.; Yamakata, A. Effect of Particle Size on the Photocatalytic Activity of WO<sub>3</sub> Particles for Water Oxidation. *J. Phys. Chem. C* **2013**, *117*, 22584–22590. [[CrossRef](#)]
36. Wu, H.; Zhang, J. Chitosan-based zinc oxide nanoparticle for enhanced anticancer effect in cervical cancer: A physicochemical and biological perspective. *Saudi Pharm. J.* **2017**, *26*, 205–210. [[CrossRef](#)]
37. Arakha, M.; Pal, S.; Samantarai, D.; Panigrahi, T.K.; Mallick, B.C.; Pramanik, K.; Mallick, B.; Jha, S. Antimicrobial activity of iron oxide nanoparticle upon modulation of nanoparticle-bacteria interface. *Sci. Rep.* **2015**, *5*, 14813. [[CrossRef](#)]
38. Naeimi, H.; Nazifi, Z.S.; Amininezhad, S.M. Preparation of Fe<sub>3</sub>O<sub>4</sub> encapsulated-silica sulfonic acid nanoparticles and study of their in vitro antimicrobial activity. *J. Photochem. Photobiol. B Biol.* **2015**, *149*, 180–188. [[CrossRef](#)]

39. Sangeetha, J.; Philip, J. Synthesis, characterization and antimicrobial property of Fe<sub>3</sub>O<sub>4</sub>-Cys-HNQ nanocomplex, with L-cysteine molecule as a linker. *RSC Adv.* **2013**, *3*, 8047–8057. [[CrossRef](#)]
40. Shaikh, S.; Nazam, N.; Rizvi, S.M.D.; Ahmad, K.; Baig, M.H.; Lee, E.J.; Choi, I. Mechanistic Insights into the Antimicrobial Actions of Metallic Nanoparticles and Their Implications for Multidrug Resistance. *Int. J. Mol. Sci.* **2019**, *20*, 2468. [[CrossRef](#)]
41. Tharani, S.; Bharathi, D.; Ranjithkumar, R. Extracellular green synthesis of chitosan-silver nanoparticles using *Lactobacillus reuteri* for antibacterial applications. *Biocatal. Agric. Biotechnol.* **2020**, *30*, 101838. [[CrossRef](#)]